Heliyon 10 (2024) e28238

Contents lists available at ScienceDirect

Heliyon

journal homepage: www.cell.com/heliyon

Research article

Cu-based thin rolled foils: relationship among alloy composition, micromechanical and antiviral properties against SARS-CoV-2

L. Lorenzetti [a,*], M. Brandolini [b,c], G. Gatti [b,c], E. Bernardi [d], C. Chiavari [e], P. Gualandi [f], G. Galliani [f], V. Sambri [b,c], C. Martini [a]

[a] Dept. Industrial Engineering (DIN), University of Bologna, Viale Risorgimento 4, 40136 Bologna, Italy
[b] Unit of Microbiology, The Great Romagna Hub Laboratory, Piazza della Liberazione 60, 47522 Pievesestina, Italy
[c] Dept. Medical and Surgical Sciences (DIMEC), University of Bologna, Via Irnerio 49, 40126 Bologna, Italy
[d] Dept. Industrial Chemistry "Toso Montanari", University of Bologna, Via Piero Gobetti 85, Bologna 40129, Italy
[e] Dept. Cultural Heritage (DBC), University of Bologna, Via degli Ariani 1, 48121 Ravenna, Italy
[f] Pietro Galliani SpA, Via Molino Malpasso 65, 40038 Vergato (BO), Italy

ARTICLE INFO

Keywords:
Respiratory tract infections
Cu-based thin foils
High-touch surfaces
Microstructure
Micromechanical properties
Antiviral efficiency (vs SARS-CoV-2)

ABSTRACT

The healthcare-associated infections (HAIs) and pandemics caused by multidrug-resistant (MDR) and new-generation pathogens threaten the whole world community. Cu and its alloys have been attracting widespread interest as anti-contamination materials due to the rapid inactivation of MDR-superbugs and viruses. Applying thin Cu-based foils on pre-existing surfaces in hygiene-sensitive areas represents a quick, simple, cost-effective self-sanitising practice. However, the influence of chemical composition and microstructure should be deeply investigated when evaluating the antimicrobial capability and durability of Cu-based materials. The effect of composition on micromechanical and antiviral properties was investigated by comparing Cu15Zn and Cu18Ni20Zn (foil thickness from 13 to 27 μm) with Phosphorous High-Conductivity (PHC) Cu. The influence of recrystallisation annealing of PHC Cu was also investigated. Microstructural characterisation was carried out by optical (OM) and scanning electron (FEG-SEM) microscopy, Energy-dispersive Spectroscopy (EDS) and Electron-Backscattered Diffraction (EBSD). The micromechanical behaviour was assessed by microhardness, microscale abrasion and scratch tests. Cu-based foils were exposed to SARS-CoV-2 for different time points in *quasi-dry* conditions (artificial sweat solution), evaluating their antiviral capability by quantitative Reverse-Transcriptase Polymerase Chain Reaction (qRT-PCR). Surface morphology, contact angle measurements and Cu release were measured. All Cu-based surfaces completely inactivated SARS-CoV-2 in 10 min: pure Cu was the best option regarding antiviral efficiency, while Cu15Zn showed the best trade-off between micromechanical and antiviral properties.

1. Introduction

Decreasing the number of deaths caused by infections represents a critical public health priority. Antibiotic- or multidrug-resistance developed by "superbugs" poses increasing threats, especially in healthcare facilities (i.e., hospitals, Intensive Care Units (ICA),

* Corresponding author. Department of Industrial Engineering, Alma Mater Studiorum, University of Bologna, Viale Risorgimento 4, 40136, Bologna, Italy.
E-mail address: luca.lorenzetti5@unibo.it (L. Lorenzetti).

https://doi.org/10.1016/j.heliyon.2024.e28238
Received 8 March 2024; Received in revised form 13 March 2024; Accepted 14 March 2024
Available online 15 March 2024

nursing homes etc.). This biohazard may easily result in severe morbidity, increased costs and prolonged length of stay in clinical settings. In this regard, Respiratory Tract Infections are globally responsible for the majority of deaths [1]. These infections, mainly caused by respiratory viruses, may induce severe lung disorders ranging from upper respiratory infections to bronchiolitis, fever, acute respiratory distress syndrome and pneumonia [2]. Likewise, the COVID-19 pandemic caused by SARS-CoV-2 (Severe Acute Respiratory Syndrome Coronavirus 2) is one of the deadliest infectious diseases in modern history. SARS-CoV-2's unique features allowed it to spread rapidly and have a catastrophic social and economic impact.

Every pathogen colonisation occurring in the upper respiratory tract could be transmitted by large droplets generated by coughs and sneezes, where a single droplet may easily comprise an infectious dose [3]. Once deposited on a surface, indirect contact transmission becomes the main route for multiresistant germs and respiratory viruses to spread and give rise to cross-contamination [2,4]. It has been reported that 4 h after inoculating a safe surrogate virus on the hands of a single employee inside of a 80-person office building, half of the surfaces and staff resulted positive to the virus [5]. Considering an average of 93 surface contact per hour, high-touch surfaces such as doorknobs, push plates on doors, bed rails (13.6 contacts/hour), bedside tables (12.3 contacts/hour) and restroom faucets represent some of the possible sources of contact-mediated infections [6,7]. These surfaces are usually manufactured in 304 stainless steel and polymers, on which SARS-CoV-2 strains exhibited resistance to inactivation for up to 48–72 h [8], or even weeks for living cells [9].

Appropriate disinfection practices can improve the prevention of contact-mediated infections; however, ineffective cleaning protocols and agents may allow residual pathogens to induce biohazards from frequently touched surfaces [10]. Vaccines represent an evolution-proof treatment to avoid outbreaks. Nevertheless, they are characterised by high time-to-market, and their storage and delivery conditions are not always feasible, especially in least-developed countries. In this scenario, the introduction of new tools which can assist infection control is essential.

Copper was the first solid metal to ever gain Environmental Protection Agency (EPA) Public Health Registration in 2008 [11] and anti-Covid approval in February 2021 [12]; no other touch surface material has this type of certification [11,12]. Since ancient times, this metal has been used for its properties in medical devices, wound care systems and water disinfection [1]. With the advent of commercially available antibiotics, Cu was gradually abandoned. Antibiotic- or multidrug-resistance has renewed interest in both pure Cu and Cu-based alloys as anti-contamination materials in hygiene-sensitive areas. Antimicrobial Cu touch surfaces can rapidly inactivate several bacteria, yeasts, and viruses responsible for HAI [2,11,13–17]: Murine Norovirus (MNV) [13], Influenza A, Human Coronavirus 229E (HuCoV-229E) [2], SARS-CoV-1, and SARS-CoV-2 [8] are just some of the respiratory viruses for which Cu and Cu alloys have a rapid inactivation effect [1,18]. Additionally, the anticontamination properties of Cu-based materials remain active even after wet and dry abrasion, re-contamination and tarnishing [19,20].

Hence, Cu-based materials may contribute significantly to a comprehensive mitigation strategy combined with standard infection control practices to effectively handle public health hazards, preventing antibiotic resistance and horizontal gene transfer among pathogens. Several pilot case studies in transportation, hospitals, long-term care, fitness and educational institutions were reported to confirm the antimicrobial efficiency in using these surfaces to retrofit existing ones, demonstrating their long-term efficiency and laying the groundwork for spreading them from laboratory studies to medical settings of common use [21].

Applying a thin Cu-based foil on pre-existing surfaces is a quick, simple and cost-effective anticontamination method, which avoids limitations due to the high costs of bulk metal and the distribution of newly manufactured components. Thin foils are easy to re-apply if optimised with proper ductility, allowing their application also on complex-geometry substrates. The mechanical properties and corrosion resistance of Cu-based foils may be finely tuned by alloying to achieve a suitable combination of properties such as workability (during manufacturing), chemical inertness and wear resistance (during service). For instance, the ratio of copper to zinc in brass can be adjusted to ensure the surface is sufficiently hard for applications such as hospital furniture and doorknobs. However, increasing the corrosion resistance of Cu alloys (resulting in long-term aesthetically acceptable surfaces), may cause a decrease in their antimicrobial efficiency [19]. Moreover, when dealing with reduced thicknesses, thin metal foils may undergo a variety of failure modes during service, such as buckling, denting, wrinkling, warping, or curling [22]. Determining mechanical properties is the first step to understand and prevent failure. Microstructural features (such as the recrystallisation degree of products which are typically produced by several hot rolling steps) affect both mechanical properties and corrosion resistance, which in turn affect antimicrobial properties through the release of Cu ions. In addition, the wettability of a surface, which is strictly related to its surface roughness, could significantly influence the persistence of a pathogen onto a substrate [23–25]. The micro- and nanoscale surface area of a sample may affect both the active sites for ion release and the probability of biofilm formation. These features are typically overlooked when solely evaluating the antimicrobial capabilities of a metal surface.

Therefore, this work addresses the relationships among microstructure, micromechanical properties and antiviral capability of Cu-based thin foils considering: (i) the effect of alloy composition (by comparing Cu15Zn and Cu18Ni20Zn with Phosphorous High-Conductivity (PHC) Cu (99.95 wt%) and (ii) the influence of recrystallisation annealing after rolling, in the case of PHC Cu. Very few studies report on the antiviral properties of Cu-based materials against Coronaviruses [2,8,26,27], and none reports on the effect of thin rolled copper alloys on SARS-CoV-2, especially with a focus on their micromechanical features.

In this work, microstructure of Cu-based foils was assessed by Electron Backscattered Diffraction (EBSD) and correlated with microhardness, microscale abrasion and scratch resistance, measured to evaluate in-service durability from a micromechanical point of view. The antiviral efficiency was tested against SARS-CoV-2 using a *quasi-dry* protocol to simulate human touch by an artificial sweat solution [24,28]. Surface morphology, contact angle measurements and quantification of Cu released from the surfaces in contact with ASW were carried out to investigate the relationship between antiviral efficiency and Cu ion release. It is worth noting that Cu alloys were tested in the form of thin foils produced in industrial environment, by tailoring processing conditions for each alloy in order to achieve a thickness in the 15–25 μm range, which makes the Cu-based foils ready for application on high-touch surfaces.

Table 1
Cu-based foils: thermo-mechanical treatments.

UNS	Acronym	Thermo-mechanical treatments	Initial thickness (μm)	Final thickness (μm)	Total thickness reduction (%)
C10300	Cu R	Cold rolling	300	24.5 ± 0.6	92
	Cu R + A	Cold rolling + recrystallisation annealing (670 °C)	300	24.1 ± 0.6	92
C23000	Cu15Zn	Cold rolling + recrystallisation annealing (670 °C)	50	27.0 ± 0.3	46
C75200	Cu18Ni20Zn	Cold rolling (with intermediate annealing (720 °C)) + recrystallisation annealing (720 °C)	200	12.6 ± 0.2	94

2. Materials and methods

2.1. Cu-based thin rolled foils

Cu-based thin foils were produced in industrial environment by Pietro Galliani SpA through thermomechanical treatments reported in Table 1. The freestanding foils used in this study, with thickness ranging from about 13 to 27 μm, were obtained via cutting from tapes with three alloy compositions:

(i) Phosphorous High Conductivity (PHC) Cu (Cu: 99.95 wt%);
(ii) Cu15Zn (brass 85/15);
(iii) Cu18Ni20Zn (nickel silver 62/18).

Cu15Zn and Cu18Ni20Zn, which showed higher mechanical properties and corrosion resistance compared to pure Cu [29] and were registered as public health anticontamination products by EPA [2,11,12], were taken into account and compared with PHC Cu.

Regarding the thermomechanical treatment conditions (Table 1), all the materials were supplied after rolling with final recrystallisation annealing, except pure PHC Cu, which was also supplied without final recrystallisation annealing. PHC Cu foils produced by rolling followed by recrystallisation annealing will be referred to as "Cu R + A", while those produced by rolling only will be referred to as "Cu R". Thermomechanical treatment conditions listed in Table 1 display variations in temperature and thickness reduction with alloy composition, required for achieving the desired thickness in the targeted range of 15–25 μm. Therefore, our work focused on assessing the properties of the finished products in terms of their suitability for the intended application.

Foil thickness was measured using a LGH-1010I–B-EH high-accuracy linear gage with a resolution of 0.01 μm and measuring accuracy of 0.2 μm by determining the average values of at least 50 measurements/sample (Table 1). At the end of the manufacturing process, Cu (R + A and R) and Cu15Zn foils were characterised by a thickness of approximately 24–27 μm, while Cu18Ni20Zn was about 13 μm thick.

The chemical composition of thin rolled foils was checked by Glow Discharge Optical Emission Spectroscopy (GD-OES, Spectruma Analitik GDA 650) with a Grimm-style glow discharge lamp in DC mode. The analysed area in each measurement was about 5 mm^2, corresponding to the internal area of the tubular anode (2.5 mm diameter).

2.2. Microstructural, micromechanical and topographic characterisation

All the samples were washed and cleaned by dipping in deionised water followed by ethanol for 5 min to remove any traces of contaminants. The thin foils (15 × 15 mm^2) were attached on a pre-formed mounting resin block using ethyl cyanoacrylate glue. To ensure that the foils were perfectly flat [30] and the glue film was thin and homogenous, the foils were pressed overnight with a glass plate.

The phase constitution of the foils was determined by X-ray diffraction (XRD), performing θ-2θ scans from 20° to 100° with a 0.02° step size and a 5 s dwell time by a Philips PW 1820 diffractometer. A Cu K alpha radiation source was used (λ = 0.15405 nm), with a 40 kV accelerating voltage and a 40 mA filament current. Texture coefficient Tc was calculated according to eqn. (1):

$$T_C = \frac{\left(\frac{I_n(hkl)}{I_0(hkl)}\right)}{\frac{1}{n}\left(\sum_{1}^{n} I_n(hkl) \Big/ I_0(hkl)\right)} \quad (1)$$

where $I_n(hkl)$ is the measured relative intensity of the reflection from the (hkl) plane, $I_0(hkl)$ is the relative intensity from the same plane in a standard reference sample and n represents the total number of reflection peaks from the sample. Tc ranges from 1 (randomly oriented sample) to n (sample with complete preferential orientation) [31].

Metallographic samples were polished by standard metallographic procedures and chemically etched by Klemm's II ((50 mL stock solution (deionised H_2O saturated with $Na_2S_2O_3$)+ 5 g $K_2S_2O_5$ [32]). Microstructural characterisation was carried out by optical (Zeiss Axio Imager A1) and electron microscopy (FEG-SEM Tescan Mira 3) equipped with electron-backscattered diffraction (EBSD) probe (Bruker eFlash HD). SEM observations were carried out using 10 kV of accelerating voltage. Ion etching was used to prepare surfaces for EBSD analysis. EBSD was performed using an acceleration voltage of 20 kV, a current ≥ 2 nA, sample at 70° tilt, working distance of

18 mm. Acquisition runs were carried out using a step size of 540 nm for Cu R + A, 270 nm for Cu R, 54 nm for Cu15Zn and 89 nm for Cu18Ni20Zn. Based on EBSD analysis, the average grain size was measured according to ASTM E2627 [33].

Free surfaces were analysed before the micro-mechanical and antimicrobial characterisation by stylus profilometry (Hommelwerke T2000, tip radius: 5 μm) using Lt = 1.25 mm (i.e., evaluation length), Lc = 0.25 mm (i.e., sampling length) according to ISO 4288-1998 [34]. Surface morphology was observed by optical (Hirox KH 7700) and scanning electron microscopy (FEG-SEM) at accelerating voltages of 10 kV.

The micromechanical behaviour was assessed by:

1) Vickers microhardness ($HV_{0.01}$), in agreement with ASTM E92-17 [35] and ISO 6507 [36];
2) Micro-scale abrasion test (MSAT, ISO 26424 [37]) using a 100Cr6 ball (Ø = 25.4 mm) with normal load = 0.05 N, an abrasive suspension of SiC (Ø ≈ 4.5 μm) with a concentration of 0.75 g/cm^3 and a sliding speed of 0.05 m s^{-1}. The schematic of MSAT is depicted in Fig. 1. The wear coefficient (m^2 N^{-1}) was measured for each foil based on the determination of the wear crater diameters by optical microscopy.

3) Constant load scratch test (Revetest XPress, CSM Instruments) with Rockwell diamond indenter (spherical tip, radius curvature: 200 μm) with a normal load of 1 N, linear speed rate = 0.2 mm s^{-1} and scratch length = 2 mm, according to ASTM G171 [38]. Scratch tests were carried out to measure the damage resistance to two-body abrasion, and it was considered complementary to quasi-static measurement methods such as Vickers micro-hardness. The constant load was selected considering that the normal force impressed by fingerprint was estimated as ranging from 0.09 N (tapping) to 1.13 N (sliding gestures: scratching and pinching) [39,40]. Hertzian maximum contact stresses were estimated along the thickness of Cu-based foils (Z-axis) by Matlab® software, according to Ref. [41]: the maximum shear stress τ_{max} induced by the scratch tests was achieved at 4.2 μm below the surface while the maximum penetration depth was 3.8 ± 0.7 μm (for Cu R + A, the softer material), confirming that the resin block below the foils was not involved in the measurements. Scratch tracks morphology was observed via optical microscopy and scanning electron microscopy. The Scratch Hardness Number HS_P was measured according to Ref. [38] on the basis of scratch width measurements by 3D-digital microscopy, in 3 zones at about the same distance along the scratch length. Penetration depth and pile-up measurements were carried out after scratching by stylus profilometry. The pile-up was measured as the height of the edge ridges and considered as a measure of plasticity. At least three repetitions were carried out for each test.

2.3. Antiviral efficiency assessment

2.3.1. Cell culture conditions

Vero E6 cell cultures were maintained in Minimum Essential Medium (MEM) with 10% heat-inactivated fetal bovine serum (FBS), 100 U/mL penicillin, 100 μg/mL streptomycin and 2 mM L-glutamine, as recommended. Cells were incubated at 37 °C in a 5% CO_2 atmosphere-enriched and humidified chamber until use [42]. Cell culture medium and supplements were all purchased from Euro-Clone SpA (Milan, Italy).

2.3.2. Virus propagation

The viral strain was isolated on cell culture from a residual clinical specimen (nasopharyngeal swab) provided for routine diagnostic purposes. Once isolated, the viral strain was titrated using the endpoint dilution method and viral titre was calculated with the Reed and Muench formula based on 8 replications for dilution and expressed as TCID50/mL (i.e., 50% tissue-culture infectious dose) [43,44].

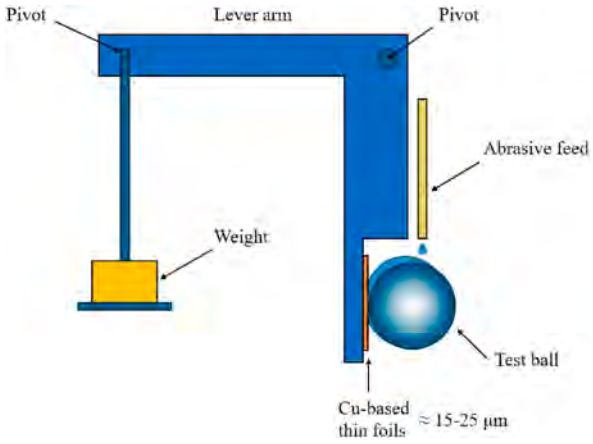

Fig. 1. Schematic of the test rig for microscale abrasive wear testing.

2.3.3. Antiviral efficiency against SARS-CoV-2

The killing rate against pathogens is strongly influenced by the protocol used to evaluate the antimicrobial efficiency of a material and, in particular, by the medium composition [9]. This work applied the *quasi-dry* protocol developed by Chang et al. [24,28] to simulate human touch conditions. Using a small amount of a transfer medium, SARS-CoV-2 virions are put directly in contact with the surface within a few seconds of deposition.

The antiviral tests were conducted using two different inoculum media: a normal saline solution (NaCl: 0.85% wt, pH ≈ 7) and an Artificial Sweat solution (ASW, prepared according to EN 1811 standard [45]).

For the viability tests, SARS-CoV-2 first interacted with the Cu-based foils and polystyrene (PS) as control sample for contact times ranging from 0 to 10 min. They were then placed in sterile tubes with 300 μL of 2% FBS-DMEM solution and vortexed for 1 min at high speed to detach biological material from the surfaces.

The whole procedure used for antiviral tests against SARS-CoV-2 is reported in Fig. 2 and summarised as follows:

1) Viral culture transferred to 5% FBS-DMEM and overnight incubation (37 °C, 5% CO_2);
2) Preparation of the artificial sweat solution (ASW, EN 1811 [45]), used within the first preparation day;
3) Dilution of SARS-CoV-2 into the inoculum (normal saline and/or ASW solution): 35 μL in 10 mL (corresponding to 10^5 TCID50/mL);
4) Cu-based foils were ultrasonically cleaned in analytical grade ethanol 5 min before the antiviral tests to prevent contamination from organic molecules;
5) Application of *quasi-dry* protocol (Fig. 2) by depositing 3 tiny droplets of 1 μL each of inoculum solution containing the pathogen for three different contact times (i.e., 2, 5, 10 min);
6) Detachment of SARS-CoV-2 after exposure by 1-min vortexing in 2% FBS-DMEM;
7) Infection of Vero E6 cell monolayers and incubation for 72 h at 37 °C, 5% CO_2;
8) SARS-CoV-2 nucleic acid quantification by Quantitative Reverse-Transcription Polymerase Chain Reaction (qRT-PCR).

Viral load was evaluated by qRT-PCR in Cu-based materials eluates (i.e., step 8 of the protocol above) and on cell cultures after 72 h of incubation to assess SARS-CoV-2's ability to replicate after contact with Cu-based surfaces. Seegene Allplex SARS-CoV-2 Extraction-Free Assay (Seegene, Seoul, South Korea) was used. The assays simultaneously amplify four genes: Envelope (E), RNA-dependent RNA Polymerase and Spike (RdRP/S, read on the same fluorescence channel) and Nucleocapsid (N). Only the Ct (Cycle threshold) of the N gene was considered for the following calculations to assess the antiviral properties of Cu-based surfaces, as it is specific for detecting SARS-CoV-2 and evolutionarily more stable.

The % activity of SARS-CoV-2 was assessed by eqn. (2):

$$\%\ activity_{SARS-CoV-2} = 1 - \frac{(Ct\ N\ gene\ sample\ 72\ h - Ct\ N\ gene\ control\ 72\ h)}{(Ct\ N\ gene\ sample\ t\ 0\ - Ct\ N\ gene\ control\ 72\ h)} \quad (2)$$

At least 3 repetitions were carried out for each test.

Antiviral activity tests were conducted according to procedures reported in the literature, involving the application of a limited inoculum volume to closely mimic fingertip touch contamination [2,13,24,28] and using qRT-PCR to determine copy number after contact with the test samples for different time points (i.e., HuCoV-229E [2], MNV [13,46]).

All activities involving the manipulation of infectious viruses were performed in a Biological Safety Level 3 (BSL-3) facility, in compliance with appropriate containment rules.

2.4. Cu release in ASW solution

Cu release was assessed according to the *quasi-dry* protocol developed by Chang et al. [24,28]: 192 ASW droplets of 2 μL each were deposited on Cu-based foils (60 × 45 mm^2) for a total volume of 384 μL. Each droplet of ASW was in contact with the solution for 10 min before being collected back with a pipette into a 4.5 mL polystyrene tube. At least 3 replicas for each condition were carried out.

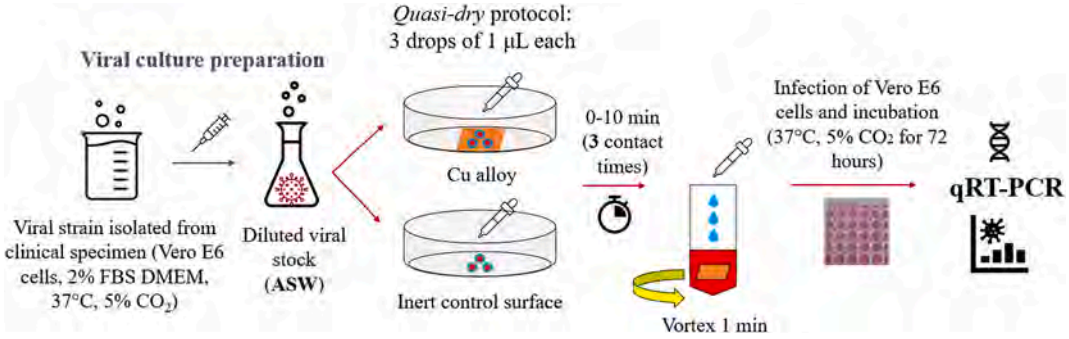

Fig. 2. Schematic of the antiviral assessment against SARS-CoV-2.

For each sample, the volume of the collected ASW droplets was checked at the end of the collection to take into account the effect of evaporation. The samples were then diluted with 1 mL of Type 1 ultrapure water (Milli-Q®, 18,2 MΩ cm) and 40 μL of 64% suprapur nitric acid (HNO_3) were added to prevent redeposition of dissolved Cu ions. The samples were stored at 2–4 °C before analysis. The exposure time was set as 10 min to achieve a fair trade-off between the maximum contact time observed to completely inactivate SARS-CoV-2 virions and the stability of the tiny droplets. Each test was carried out using ASW as inoculum medium without dispersed virions. Cu ions released in ASW solution were analysed by Agilent Technologies 421 Microwave Plasma Atomic Emission Spectroscopy (MP-AES) and quantified by considering the peak intensity at the wavelength of 324.76 nm. Calibration standards of Cu were prepared using concentrations of 1, 2, 5, 10, 20 ppm. At the same time, blank reference solutions (ASW only) were analysed and used to adjust Cu background concentrations for each condition.

Contact angle measurements were conducted to examine the surface wettability of the Cu-based metal surfaces by using a Kruss model DSA30 Drop Shape Analyser. An ASW droplet (2 μL) was illuminated when dispensed on the surface and immediately captured by a high-resolution camera. The contact angle was determined as the average value of 3 measurements. Each measurement was performed 5 s after deposition and 10 min later.

3. Results and discussion

3.1. Morphological and microstructural features

The chemical composition of each Cu-based material is reported in Table 2, together with nominal data for the UNS alloy types with closest composition.

According to these chemical compositions, all the investigated Cu-based alloys displayed a single-phase α-Cu Face Centered Cubic (FCC) structure, as shown by XRD analysis (Fig. 3).

The free surface morphologies of all the samples (Fig. 4a–h) were characterised by (i) macroscopic rolling marks (horizontal lines in the images of Fig. 4a–h), as well as microscale wrinkles (perpendicular to rolling marks, Fig. 4e–h). This type of microscale wrinkles is known to initiate near strain gradients at selected points on the foil during lamination or further processing due to non-uniform loading conditions [47]. Moreover, given the low thickness of the foils, they were prone to handling damage such as bending, wrinkling, denting and micro-buckling. These phenomena were more evident for Cu R + A (i.e. the softer foil) and Cu18Ni20Zn (i.e. the thinner foil, Table 1). Cu R and Cu15Zn were less prone to processing and handling damages in comparison with Cu R + A (which underwent complete recrystallisation, as discussed afterwards), likely thanks to a higher strain-hardening rate. Cu18Ni20Zn (Fig. 4h) was the only sample showing the presence of slip bands already on the free surface, due to the highly localised deformation induced by its thickness reduction below 15 μm.

The different deformation behaviour and thickness of the foils affected the surface roughness of the Cu-based foils (Table 3): Rq (root mean square roughness, μm) and Rz (ten-point height, μm) values showed that the highest surface roughness was attained by Cu18Ni20Zn sample, followed by rolled and annealed Cu (R + A), while rolled Cu R and Cu15Zn displayed the lowest roughness. On the one hand, the low deformability of Cu15Zn and Cu R due to high strain-hardening led to low surface roughness. On the other hand, the lowest thickness of Cu18Ni20Zn favoured the formation of macro-wrinkles, leading to the highest Rq and Rz values.

Fig. 5 shows the main microstructural features of Cu-based foils, based on optical micrographs, SEM images and EBSD grain distribution maps. In the case of pure Cu samples (Fig. 5a–f), the grains were firstly flattened by rolling (Cu R, Fig. 5a–c), and after subsequent annealing (Cu R + A) new equiaxed grains were formed (Fig. 5d–f). This becomes more evident when comparing the isometrical SEM images in Fig. 5b and e: Cu R (Fig. 5a-c), not subjected to recrystallisation annealing, displayed highly elongated grains towards the rolling direction with a flat, ellipsoidal shape in the plane normal to the rolling direction. On the other hand, Cu R + A (Fig. 5d–f) showed equiaxed recrystallised grains with annealing twins. While micro-kinks and annealing twins were detected for both Cu R + A (Fig. 5e) and Cu18Ni20Zn (Fig. 5m), slip lines were observed for all the samples, even after recrystallisation annealing, likely because of the primary extensive strain-hardening. The slip marks also formed on Cu15Zn (Fig. 5h) sample but to a lesser extent, likely due to its lower total thickness reduction % than the others [48].

EBSD grain distribution maps (Fig. 5 c, f, i, n) show that alloying led to grain refinement in Cu15Zn and Cu18Ni20Zn (as shown by average grain size values in Table 4) as well as to delayed recrystallisation. Annealing led to grain coarsening in the case of pure Cu, while the slightly lower grain size of Cu15Zn compared to Cu18Ni20Zn may be due to the intermediate annealing treatments (Table 1) combined with the highest annealing temperature used for Cu18Ni20Zn foils (i.e., 670 °C vs 720 °C). Moreover, the higher

Table 2
Chemical composition of Cu-based foils (wt.%): comparison of experimental results (GD-OES) with nominal composition [29].

UNS		Elements (wt %)			
		Cu	Zn	Ni	Others
C10300	Cu PHC	99.86 ± 0.01	0.032 ± 0.002	0.0010 ± 0.0005	0.03
	Nominal	*99.95*	-	-	*0.001–0.005*
C23000	Cu15Zn	85.33 ± 0.80	14.42 ± 0.67	–	0.25
	Nominal	*84–86*	*14–16*	-	*0.05*
C75200	Cu18Ni20Zn	60.23 ± 0.20	20.74 ± 0.13	18.15 ± 0.13	0.86
	Nominal	*63.0–66.5*	*16.5–19.5*	*16.5–19.5*	-

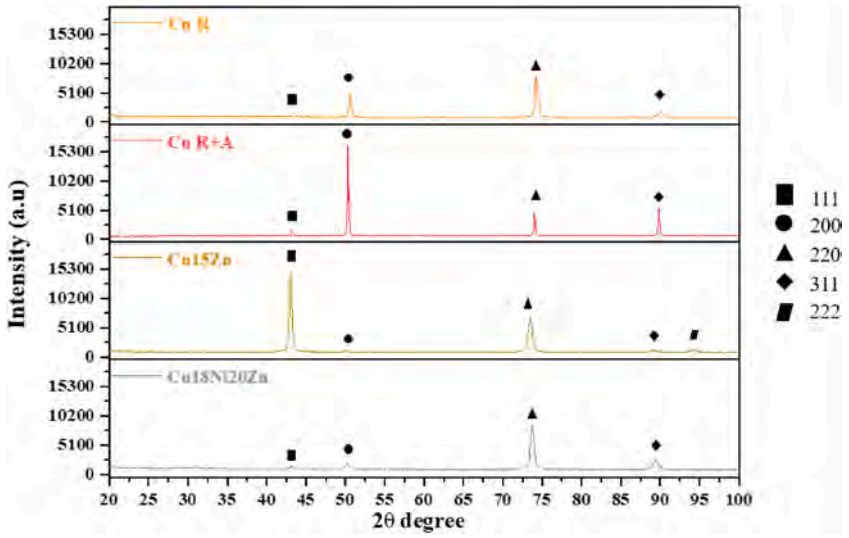

Fig. 3. Indexed θ–2θ X-ray diffraction patterns, representative of the through-thickness phase composition of Cu-based materials.

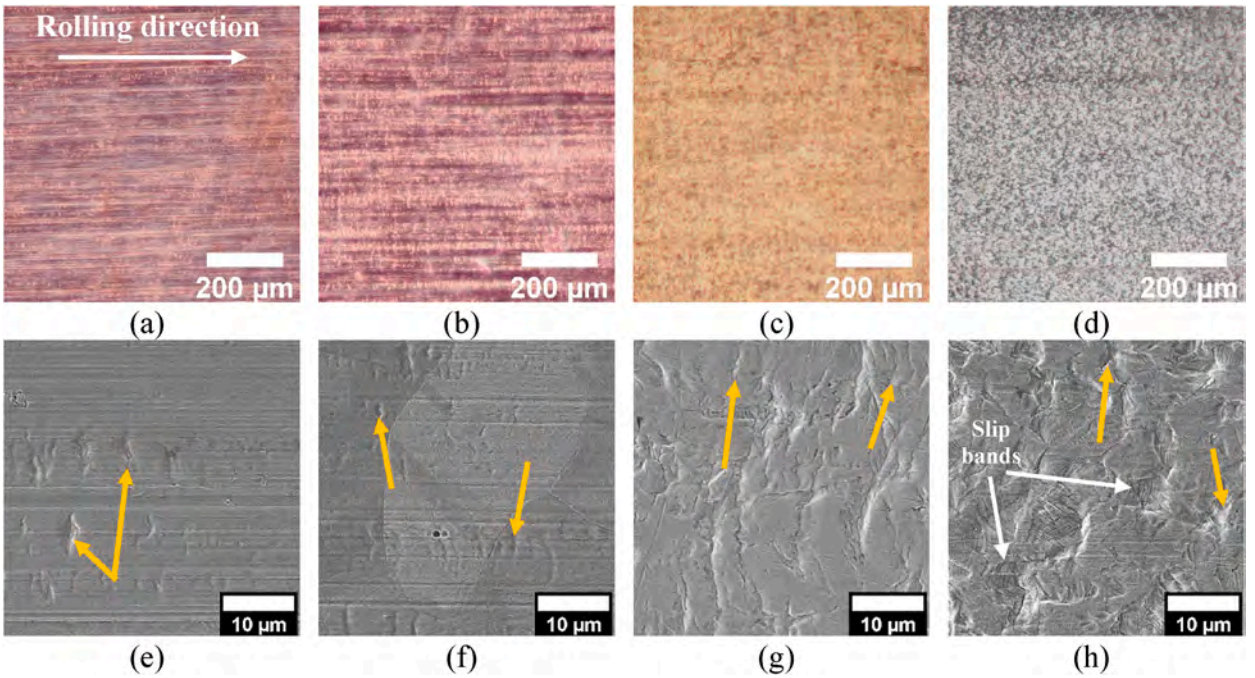

Fig. 4. (a-d) Optical and (e-h) secondary electron micrographs of the free surface morphology of Cu-based materials: (a, e) Cu PHC R; (b, f) Cu PHC R + A; (c, g) Cu15Zn; (d, h) Cu18Ni20Zn. Yellow arrows indicate micro-wrinkles (perpendicular to horizontal marks along the rolling direction) and white arrows indicate slip bands. (For interpretation of the references to colour in this figure legend, the reader is referred to the Web version of this article.)

deformation rate of Cu18Ni20Zn compared to Cu15Zn could be responsible for decreased nucleation and coarsening time of newly-recrystallised grains in Cu18Ni20Zn.

Partial recrystallisation was confirmed by Tc values from XRD analysis: the deviation of Tc values from the unitary value for the (220) plane demonstrates a preferential (220) orientation for all the samples except Cu R + A, as shown in Table 5.

Also EBSD Pole Figures (PFs, Fig. 6) reveal a preference for rolling plane orientation {110} toward the rolling direction (except for Cu PHC R + A). The absence of preferential (220) orientation in Cu R + A was probably observed since this was the only sample undergoing complete recrystallisation after annealing, because of its lower recrystallisation temperature (which can be around 140 °C or lower, depending on purity and the extent of cold working [49]). Conversely, in alloyed samples, partial recrystallisation left a

Table 3
Linear surface roughness parameters (Rq, Rz, ISO 4288-1998 [34]) of the Cu-based materials.

Sample	Rq (nm)	Rz (nm)
Cu R	95 ± 10	658 ± 148
Cu R + A	180 ± 54	1097 ± 551
Cu15Zn	93 ± 8	688 ± 80
Cu18Ni20Zn	292 ± 183	1172 ± 479

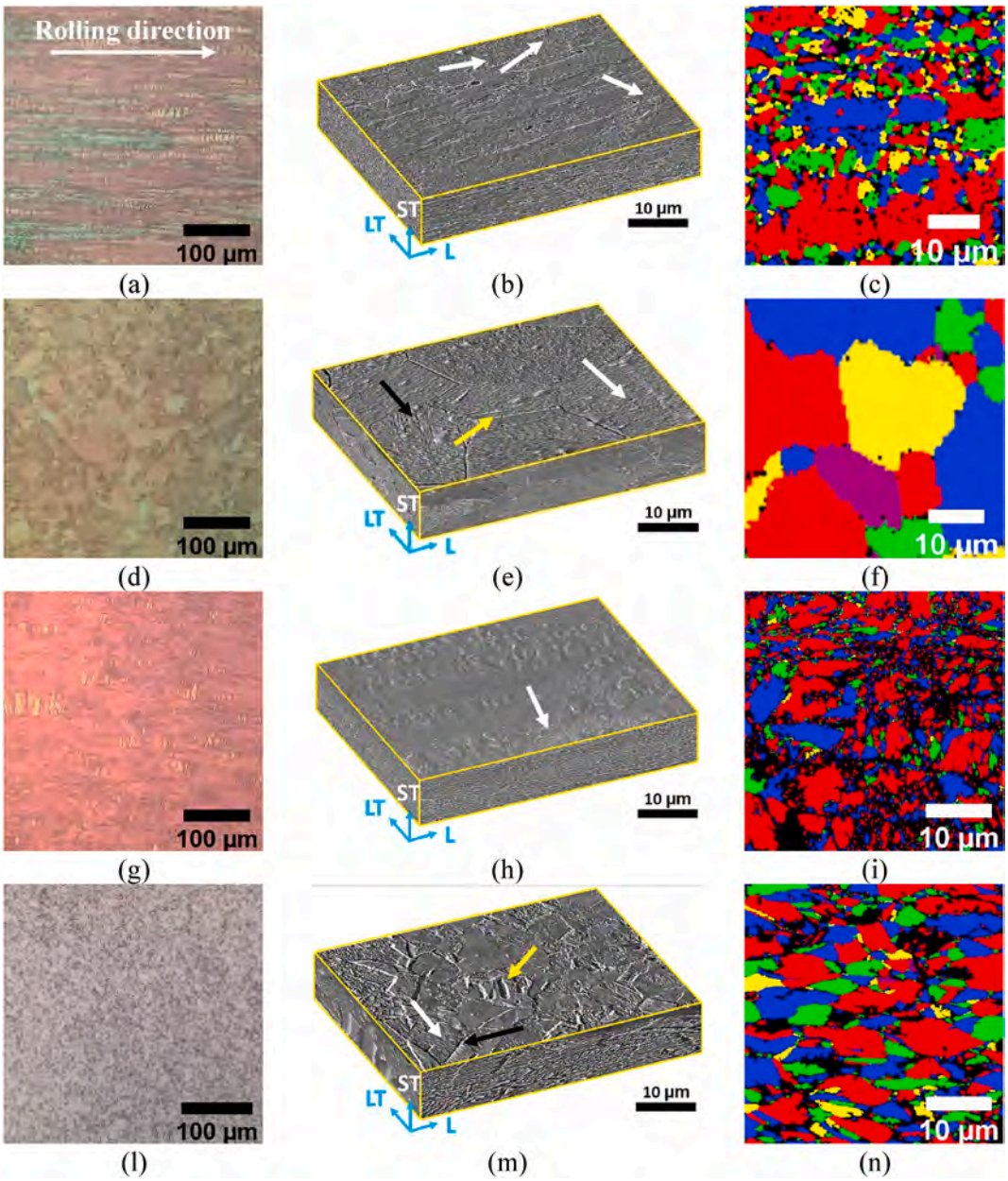

Fig. 5. (a, d, g, l) Top-view of the rolling plane: optical micrographs after chemical etching with Klemm's II reagents, (b, e, h,m) 3D reconstructions (SEM images) and (c, f, i, n) EBSD grain distribution maps (rolling plane) of the Cu-based materials: (a, b, c) Cu R; (d, e, f) Cu R + A; (g, h, i) Cu15Zn; (l, m, n) Cu18Ni20Zn. White arrows indicate microbands (i.e., aggregation of slip lines) formed by intensive strain hardening; yellow arrows indicate twin bands and black arrows indicate kink bands. (For interpretation of the references to colour in this figure legend, the reader is referred to the Web version of this article.)

Table 4
Average grain size of the Cu-based materials, determined by EBSD according to ASTM E2627 [33].

Sample	Average grain diameter (μm)
Cu R	5.4 ± 0.7
Cu R + A	17.7 ± 4.7
Cu15Zn	1.5 ± 0.1
Cu18Ni20Zn	2.6 ± 0.1

significant fraction of highly deformed grains, characterised by a high number of slip bands and elongated grains of α-solid solution with fibre texture towards rolling direction, as observed also for Cu R which was not annealed after rolling. For these samples, EBSD {100}- and {111}-PFs (Fig. 6a, c, d) showed close agreement with established literature pattern for 95% cold rolled medium-to-low Stacking Fault Energy (SFE)-FCC metals as pure Cu and Cu30Zn revealing the presence of the following orientation components: copper {112}(111), S {123}(634) and brass {110}(112) [50]. Conversely, the typical copper-type rolling texture tended to disappear after annealing pure Cu R + A (Fig. 6b), confirming the occurrence of recrystallisation, as already observed in Ref. [51] for cold-rolled copper sheets after annealing treatment.

3.2. Micromechanical behaviour

The mechanical behaviour of Cu-based thin rolled foils was firstly evaluated by Vickers microhardness measurements (i.e., $HV_{0.01}$, Fig. 7a). Cu15Zn showed the highest microhardness (201 ± 11), followed by Cu18Ni20Zn (181 ± 17), Cu R (140 ± 5) and Cu R + A (56 ± 1). The high $HV_{0.01}$ showed by Cu15Zn and Cu18Ni20Zn can be attributed to the combined effect of grain refinement and solid-solution strengthening. Grain refinement was highlighted for both alloys by EBSD grain distribution maps (Fig. 5c, f, i, n) as well as by grain size values in Table 4. In the case of Cu15Zn, grain refinement probably played a more important role than solid-solution strengthening because, even though this alloy was characterised by a lower concentration of alloying elements and lower total thickness reduction than Cu18Ni20Zn, it showed slightly higher $HV_{0.01}$ than Cu18Ni20Zn. Moreover, the influence of the glue film on the final $HV_{0.01}$ measurement may have disfavoured nickel silver and could not be excluded, given its low thickness (according to ASTM E92-17). Considering pure Cu, complete recrystallisation induced by the final annealing treatment (i.e. Cu R + A) led to the lowest $HV_{0.01}$ values, due to grain coarsening after recovery and full recrystallisation; solid-solution strengthening not occurring in pure Cu. The onset of complete recrystallisation after annealing of Cu R + A is clearly shown by EBSD P Fs (Fig. 6), and texture coefficient Tc determined by XRD (Table 5), whilst grain coarsening is demonstrated by grain distribution maps in Fig. 5c, f, i, n, and grain size values in Table 4. On the other hand, Cu R showed higher $HV_{0.01}$ values in comparison with Cu R + A thanks to the effect of strain-hardening induced by rolling without final recrystallisation annealing. Overall, the isothermal annealing treatment induced microstructural variations resulting in a softening effect of about 60% in Cu samples, thereby yielding comparable $HV_{0.01}$ values to those observed in Refs. [51,52] for fully recrystallised pure Cu.

To further characterise the resistance of the Cu-based foils to permanent deformation and third-body abrasion, constant load scratch tests were carried out. Scratch Hardness Numbers (HS_{1N}) values (Fig. 7b) measured by constant load scratching were in agreement with the $HV_{0.01}$ measurements, confirming the trend observed for quasi-static Vickers microhardness measurements. Penetration depths after scratching (Fig. 7c) showed that the harder the material, the lower the damage: the more scratch-resistant Cu-based alloy was Cu15Zn, followed again by Cu18Ni20Zn, Cu R and Cu R + A (i.e., the softer material due to full recrystallisation and no solid-solution strengthening). Therefore, the reasons for the observed trend can be ascribed to those previously discussed for $HV_{0.01}$ measurements. In fact, a plasticity-dominated behaviour was observed during scratching, with material removed from the centre of the track to form ridges along the edges (Fig. 8). Therefore, pile-up quantification (Fig. 7d) was also carried out to assess the damage of the Cu-based samples induced by scratching, confirming the inverse correlation between scratching damage and hardness (Fig. 7a–c and d). This type of correlation is explained by the morphology of scratch tracks (Fig. 8), which highlighted ploughing as the main wear mechanism. Progressive material removal smoothed out the bottom of the tracks, where the original wrinkled texture of the thin foils' surface (Fig. 4e–h) nearly disappeared in comparison to the unscratched surface. Also, the sides of the tracks appeared smooth and straight without cracks, suggesting a plasticity-dominated behaviour with no brittle failures for all the foils, as already observed for Cu micro-scratching [53].

The results of MSAT, carried out to assess three-body abrasion resistance of the Cu-based foils are reported in Fig. 7e (i.e.,

Table 5
XRD texture coefficients (Tc).

Sample	Texture coefficient Tc (*hkl*)				
	(111)	(200)	(220)	(311)	(222)
Cu R	0.02	0.63	3.09	0.26	–
Cu R + A	0.07	1.41	1.59	1.88	0.05
Cu15Zn	1.44	0.05	2.63	0.12	0.76
Cu18Ni20Zn	0.03	0.16	3.10	0.70	–

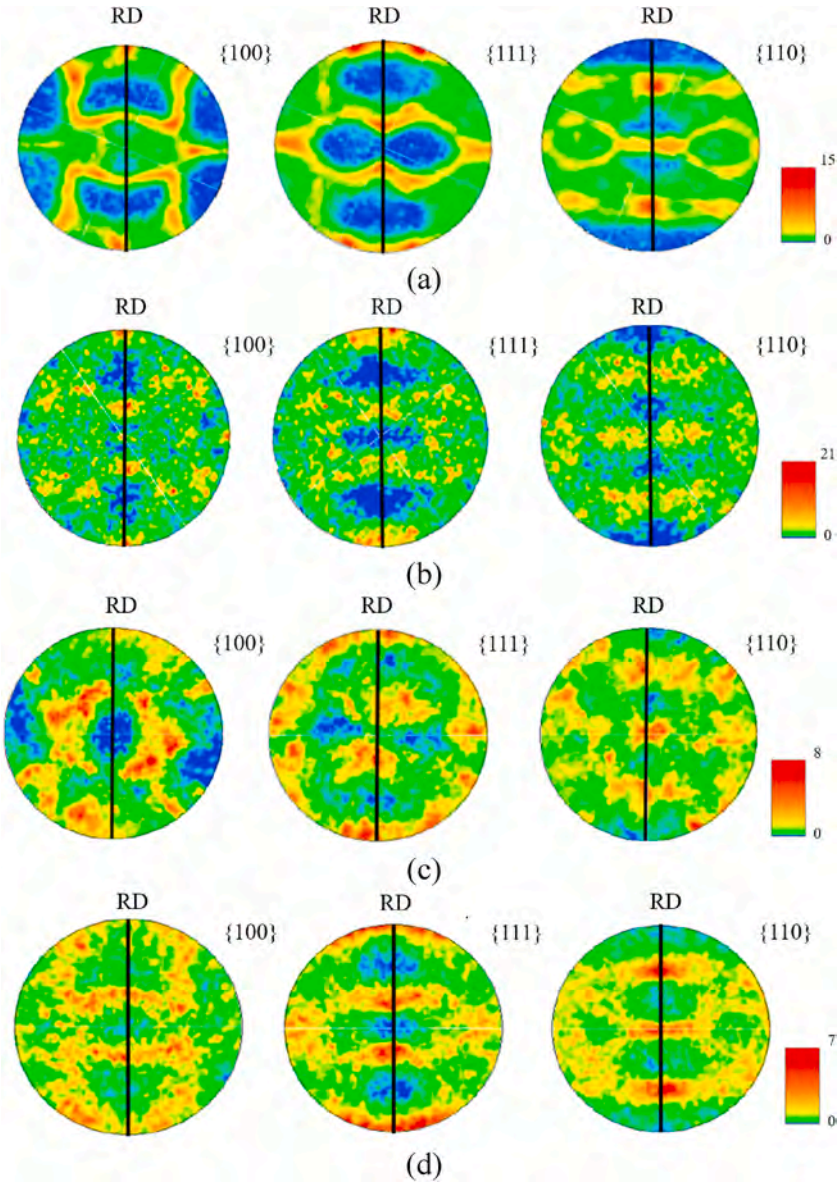

Fig. 6. Stereographic projection representation of {100}, {111}, {110} pole figures of the Cu-based materials: (a) Cu R, (b) Cu R + A, (c) Cu15Zn, (d) Cu18Ni20Zn. The scale at the bottom right for each pole figure reports the coldest colour to the lowest pole density value and the warmest colour to the highest pole density value. (For interpretation of the references to colour in this figure legend, the reader is referred to the Web version of this article.)

dimensional abrasive wear coefficient *k*). As previously observed for scratch tests, simulating dry two-body abrasion, also for MSAT the wear coefficient was inversely correlated to both $HV_{0.01}$ and HS_{1N}: Cu15Zn, the hardest and most scratch-resistant foil showed the lowest wet three-body abrasion rate. On the other hand, Cu R showed a lower *k* value than Cu R + A, thanks to strain-hardening during rolling without final recrystallisation annealing. Unfortunately, it was not possible to obtain reliable results for the Cu18Ni20Zn foils, due to their very low thickness: wear craters always perforated the whole foil even at the lowest applicable load (i.e., 0.05 N).

To summarize, Cu15Zn and Cu18Ni20Zn showed the highest hardness, scratch and abrasion resistance thanks to grain refinement due to partial recrystallisation and solid solution strengthening. Conversely, Cu R + A showed the lowest micro-mechanical performance due to full recrystallisation (demonstrated by the disappearance of the texture derived from primary rolling (PFs in Fig. 6 and Tc in Table 5)) and grain coarsening, as discussed in Section 3.1. However, the high plastic deformability of Cu R + A may help apply the thin foil during service.

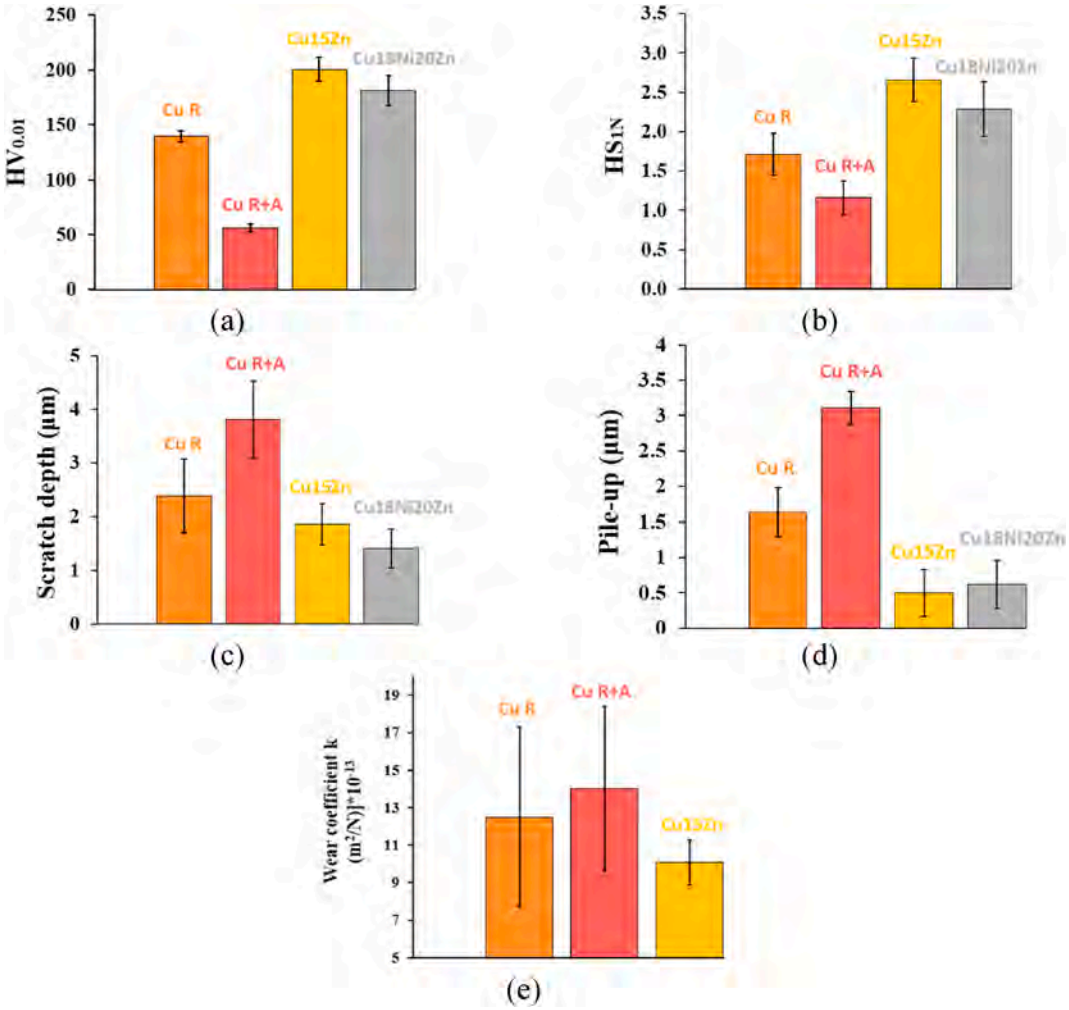

Fig. 7. (a) $HV_{0.01}$; (b) Scratch Hardness Number (HS_{1N}); (c) pile-up and (d) penetration depth obtained by stylus profilometry measurements of the scratch track and (e) wear coefficient *k* obtained from micro-scale abrasion tests (MSAT).

3.3. Antiviral capability assessment & Cu release

As reported in §2.3.3, the *quasi-dry* protocol [24,28] was used to assess the antiviral efficiency of Cu-based surfaces against SARS-CoV-2. This method was reported to reliably simulate real surface use conditions [24]. Applying a limited solution volume as SARS-CoV-2 inoculum allows the liquid to dry rapidly, placing the microbe in direct contact with the Cu-based surface.

The *quasi-dry* tests were firstly carried out using a normal saline solution (NaCl: 0.85% wt, pH ≈ 7) as inoculum medium: the total inactivation time or zero point for each Cu-based foil is reported in Table 6.

The results in saline solution allowed a first assessment of the inactivation time, showing that all the Cu-based foils are able to inactivate SARS-CoV-2 faster than the control surface and within 10 min of exposure. Moreover, these data indicate that alloy addition delays inactivation, as previously demonstrated by Refs. [2,13].

The kinetics of SARS-CoV-2 activity, as determined by equation (2), were examined with more detail, in more closely representative conditions, through exposure to an artificial sweat inoculum solution (ASW) in *quasi-dry* conditions. The results are illustrated in Fig. 9. Similarly to other studies based on the application of a small amount of buffering medium [2,13], a fast viral inactivation was observed: complete reduction of SARS-CoV-2 activity was observed after 2 min for pure Cu and 10 min for all the Cu-based foils. Conversely, on the PS control surface SARS-CoV-2 was inactivated after 30 min. These values are lower than those obtained by other methods, which however, deal with higher amounts of pathogen solution [46]. The faster inactivation in our case may be attributed to the generation of a higher concentration of Cu ions in the lower inoculum volume [54], as also observed by Refs. [2,13], where the reduction of inoculum volume led to a decrease in the inactivation time of HuCoV-229E and MNV on dry copper surfaces.

The lowest inactivation time towards SARS-CoV-2 was shown by pure Cu, which, regardless of microstructure, inactivated the virus between 2 and 5 min; negligible differences were detected between the antiviral behaviour of Cu R and Cu R + A. Hence, recrystallisation annealing did not affect the antiviral activity against SARS-CoV-2. On the other hand, the alloy composition played a crucial

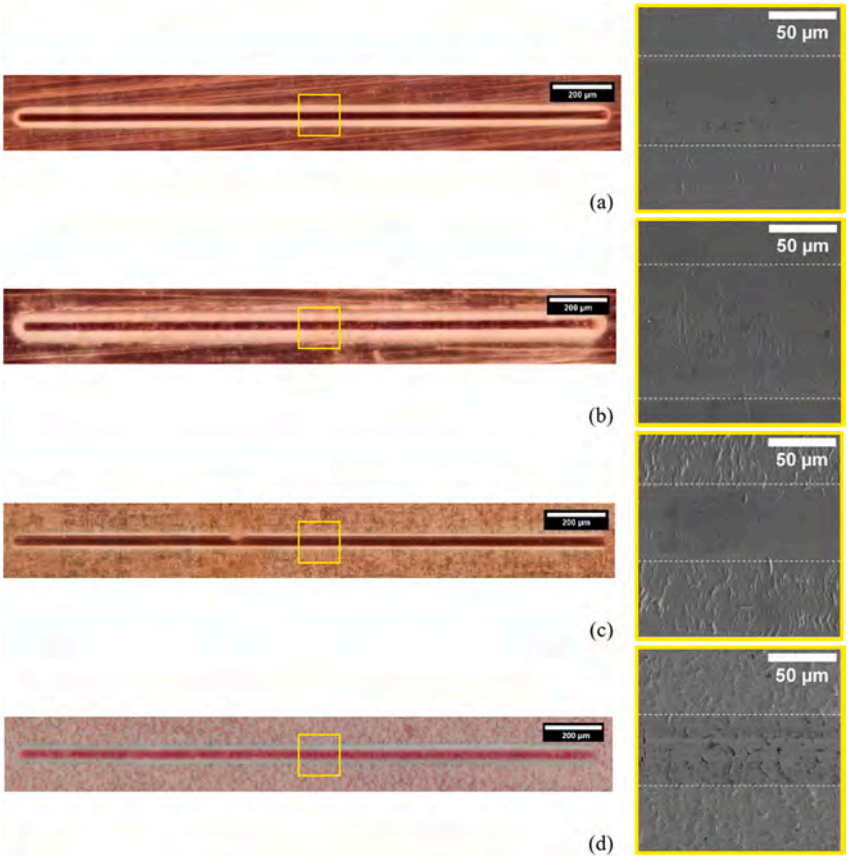

Fig. 8. Morphology of the scratch tracks (normal load: 1 N).General view (OM) and high-magnification details (SEM): (a) Cu R; (b) Cu R + A; (c) Cu15Zn; (d) Cu18Ni20Zn.

Table 6
List of inactivation times (i.e., zero point) against SARS-CoV-2 on Cu-based surfaces (R: rolling without final annealing; R + A: rolling followed by recrystallisation annealing) from the *quasi-dry* tests using normal saline solution as inoculum medium.

Sample	Manufacturing cycle	Zero point (min.)
Cu R	R	1
Cu R + A	R + A	3
Cu15Zn	R + A	≤10
Cu18Ni20Zn	R + A	10
Polystyrene	–	>10

role in determining the antiviral efficiency of Cu-based samples. The rate of viral inactivation was proportional to the Cu content of the tested alloy, as observed elsewhere [2,13]: pure Cu (≈99.9%wt Cu) was the most active material, followed by Cu15Zn (≈85%wt Cu) and lastly by Cu18Ni20Zn (≈60%wt Cu). While Cu18Ni20Zn already exhibited activity against enveloped viruses such as MNV [13] and Baculovirus [55], its antiviral efficacy was found to be comparatively lower than that of Cu15Zn, as previously observed in Ref. [13].

In general, Cu inactivates pathogens through a combination of complex synergic processes. However, the overall mechanism can be summarised in a schematic sequence of events referred to "Contact Killing" [11]: (1) direct Cu dissolution from the surface to the outer membrane of the pathogen with first external damages; (2) formation of leakage cavities in the outer membranes with losses of water and vital substances, causing loss of structural integrity; (3) formation of Reactive Oxygen Species (ROS) through redox reactions mediated by Cu, producing additional damages and (4) degradation of genomic and plasmid DNA. Specifically, viral inactivation (i.e., HuCoV-229E) is primarily due to Cu ions release, while the effect of ROS is minimal, even though ROS generation plays a more significant role as the percentage of Cu in the alloy decreases [2].

In order to better understand the antiviral activity of Cu-based foils, Cu release from the Cu-based foils was assessed according to the *quasi-dry* protocol in ASW solution [24,28], since dissolved Cu ions are considered the main factor affecting the Contact Killing

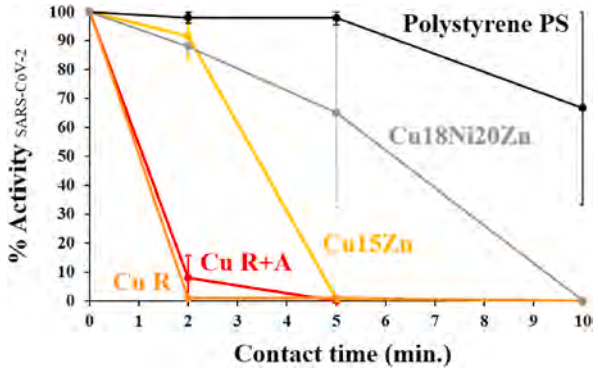

Fig. 9. % Activity of SARS-CoV-2 as a function of contact time (0–10 min) in ASW solution; a polystyrene surface (i.e., PS) was always used as the benchmark.

mechanism [12,36,38]. As shown by Fig. 10, the highest Cu release in ASW was shown by pure Cu, in agreement with the higher antiviral activity shown by Cu R and Cu R + A (Fig. 9).

Cu15Zn displayed a slightly lower amount of dissolved Cu (2.27 ± 0.22 ppm) compared to Cu18Ni20Zn (4.09 ± 0.02 ppm), as already reported in Ref. [56], despite its higher antiviral activity against SARS-CoV-2 (Fig. 9). Therefore, global Cu ion release is probably not the only factor affecting the antiviral activity of Cu alloys. There can be several reasons why Cu15Zn showed higher antiviral activity than Cu18Ni20Zn. Firstly, Zn preferentially dissolves from α-brasses [57] and has an intrinsic antimicrobial activity, synergistic with Cu [46], whilst Ni has low intrinsic antimicrobial properties [58,59]. Secondly, MP-AES did not distinguish between the type of Cu ions (i.e., Cu (I or II)) released from the surfaces. During virus exposure to Cu (I) and Cu (II), fragmentation of the envelope, dispersion of surface spikes, and virus particle aggregation were observed [1,2,13]. Concurrently, the production of ROS induced by Cu ions was reported to contribute to irreversible degradation of the virus [11]. In viral assays, Cu (I) ions were found to inactivate Influenza virus by inducing ROS onset, while Cu (II) exhibited activity against both enveloped and non-enveloped viruses [18,60]. Warnes et al. [2,13] reported that Cu (I) is primarily responsible for the viral inactivation of MNV, with Cu (II) playing an essential but short-term role. Additionally, according to Warnes et al. [2], brasses showed higher activity against HuCoV-229E compared to Cu–Ni alloys, attributed to an increase in Cu (I) release and subsequent ROS formation [2]. In our work, even though Cu18Ni20Zn showed a slightly higher global Cu ion release in ASW, establishing which was the dominant Cu ion species was not feasible. However, we took into account surface roughness and its impact on both wettability and adhesion of pathogens. As reported in literature [28,61], an increase in the amplitude of asperities and valleys may favour both the attachment of viruses or bacteria and close contact between the pathogen and sites from which Cu ions can be released, leading to faster inactivation. Microscopic grooves or scratches of a similar size to the pathogen may increase the probability of adhesion and binding potential [62]. In terms of wettability, surface roughness affects the contact angle (CA) between a buffering medium and a metal surface, resulting in different drying rates of the ASW micro-droplets when applied on it. For this reason, the CA formed by depositing 2 μL-ASW droplets on the investigated surfaces were determined (Fig. 11).

The capacity of a liquid to wet a surface is a complex process related to different parameters (i.e. surface topography, pH, temperature, interfacial energy, surface chemistry). Typically, the higher the surface roughness, the higher the hydrophilicity (wettability) of a surface, indicated by a lower CA [24,63]. CA measurements of ASW droplets on Cu-based foils showed that the higher the surface roughness (Table 3), the lower the CAs. Among the Cu-based materials, the highest CA value was attained by the smoothest Cu15Zn, indicating it was the most hydrophobic surface, generally observed as the less prone to pathogen adhesion [25]. Moreover, a higher evaporation rate of the ASW droplets may be supposed based on the larger CA value of Cu15Zn, because a higher surface area of the droplet was exposed to the atmosphere. Decreasing the inoculum volume may have locally increased the Cu ion concentration within the droplets during the tests, leading to a faster viral inactivation compared to Cu18Ni20Zn. The different extent of evaporation was confirmed by the variation of CA (i.e., ΔCA) of ASW droplets after 10 min on the different Cu-based surfaces (Fig. 12): the higher ΔCA was shown by Cu15Zn (≈28.2°), while ASW droplets onto Cu18Ni20Zn surface decreased their CA of about 16.9°. Hence, the phenomena occurring in single droplets affected the tests: a higher evaporation rate of SARS-CoV-2-containing ASW might have contributed to increase the inactivation efficiency of the Cu15Zn surface because of the increased Cu ion concentration within single droplets.

Therefore, the higher inactivation rate of Cu15Zn in comparison to Cu18Ni20Zn can be attributed to a combination of synergistic metal activity (Cu + Zn), selective Cu ion-type release, and evaporation-related effects.

4. Conclusions

The present work addresses the relationships among microstructure, micromechanical properties and antiviral capability of Cu-based thin foils considering: (i) the effect of alloy composition (by comparing Cu15Zn and Cu18Ni20Zn with Phosphorous High-Conductivity (PHC) Cu (99.95 wt%) and (ii) the influence of recrystallisation annealing after rolling, in the case of PHC Cu (considering both the strain-hardened (R) and recrystallised (R + A) condition). The microstructure of Cu-based foils was assessed by

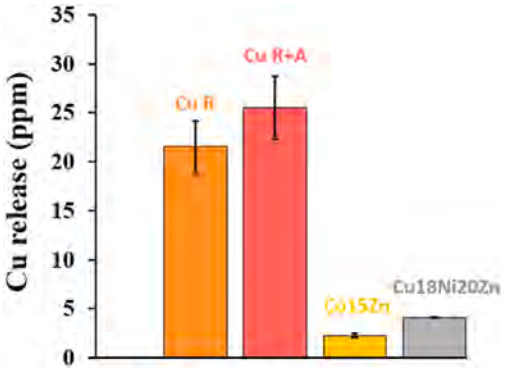

Fig. 10. Cu release amount in artificial sweat (ASW) droplets after 10 min of exposure in *quasi-dry* conditions.

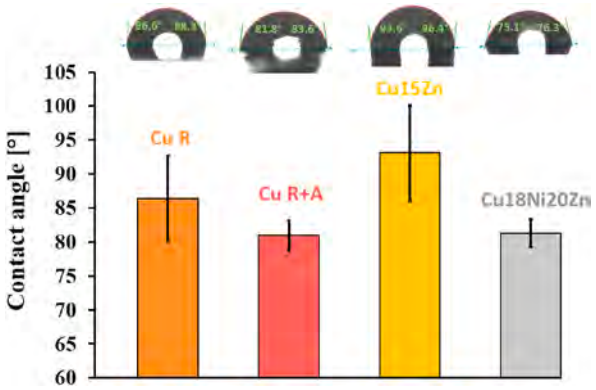

Fig. 11. Contact angle [°] of ASW droplets on different Cu-based surfaces after 5 s of deposition.

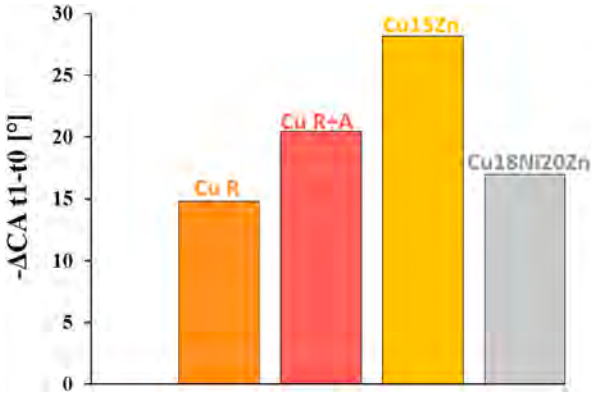

Fig. 12. Contact angles (CAs) variation of ASW droplets during time (after 10 min of contact with the Cu-based surfaces).

Electron Backscattered Diffraction (EBSD) and correlated with microhardness, microscale abrasion and scratch resistance, measured to evaluate in-service durability from a micromechanical point of view.

Cu-based foils were exposed to SARS-CoV-2, applying the *quasi-dry* protocol in artificial sweat solution (ASW) for different time points, evaluating their antiviral capability by quantitative Polymerase Chain Reaction (qRT-PCR).

Cu release assays, surface morphology and contact angle measurements were performed to better understand antiviral activity of the Cu-based thin foils.

The following conclusions can be drawn from this work:

- A Cu single-phase α structure characterised all the Cu-based materials, which showed different degrees of recrystallisation according to the thermo-mechanical treatment sequence. Recrystallised Cu (R + A) consisted of coarse equiaxed grains containing

annealing twins. Strain-hardened Cu (R) highlighted highly elongated grains towards the rolling direction. Adding Zn and Ni delayed recrystallisation and hence grain coarsening, leading to grain refinement in Cu18Ni20Zn and Cu15Zn samples;

- Both chemical composition and microstructure had an influence on the micromechanical properties of Cu-based thin rolled foils: Cu15Zn sample showed the highest $HV_{0.01}$ Vickers microhardness followed by Cu18Ni20Zn, Cu R and Cu R + A. The same trend was observed for scratch resistance, where a plasticity-dominated behaviour was revealed, as well as for three-body abrasion. Cu15Zn and Cu18Ni20Zn samples showed the highest resistance to plastic deformation thanks to the combined effect of grain refinement and solid-solution strengthening. Conversely, Cu R + A showed the lowest resistance due to grain coarsening and no solid-solution strengthening.
- All Cu-based surfaces completely inactivated SARS-CoV-2 in max. 10 min. The chemical composition was the main factor affecting the antiviral efficiency of Cu-based thin rolled foils: the lowest inactivation time was shown by pure Cu, regardless of its microstructure (R or R + A). The inactivation time was directly related to the Cu content in the alloy: Cu > Cu15Zn > Cu18Ni20Zn. Even though Cu release plays a crucial role in determining the antiviral activity, also surface features should be taken into account when using the *quasi-dry* protocol as evaluation method. In particular, surface roughness (influenced by composition, processing sequence and hence microstructure, as well as by foil thickness) was inversely related to the contact angle in ASW: the lower the surface roughness, the higher the hydrophobicity (Cu15Zn < Cu R < Cu R + A < Cu18Ni20Zn). While for pure Cu the concentration of released Cu was directly correlated with antiviral activity, the higher antiviral activity of Cu15Zn compared to Cu18Ni20Zn was explained based on: (i) synergistic action of Cu and Zn (ii) selective Cu ion release: Cu (I) > Cu (II), (iii) evaporation-related effects of the SARS-CoV-2-containing inoculum droplets.

All the materials are good candidates for application on high-touch surfaces. Based on these results, pure Cu is the most effective option for short-term applications where a frequent turnover and an easy replacement of damaged foils are expected. When foil replacement is difficult or cannot be frequently carried out, Cu15Zn thin foils provide the best trade-off between micromechanical and antiviral efficiency against SARS-CoV-2.

Data availability statement

Data supporting this study will be made available on request.

CRediT authorship contribution statement

L. Lorenzetti: Writing – review & editing, Writing – original draft, Methodology, Investigation, Data curation, Conceptualization. **M. Brandolini:** Writing – review & editing, Validation, Methodology, Investigation. **G. Gatti:** Writing – review & editing, Validation, Methodology, Investigation. **E. Bernardi:** Writing – review & editing, Methodology. **C. Chiavari:** Writing – review & editing. **P. Gualandi:** Writing – review & editing, Resources. **G. Galliani:** Writing – review & editing, Resources. **V. Sambri:** Writing – review & editing, Conceptualization. **C. Martini:** Writing – review & editing, Visualization, Supervision, Project administration, Funding acquisition, Conceptualization.

Declaration of competing interest

The Authors declare that they have no known competing financial interests or personal relationships that could have appeared to influence the work reported in this paper.

Therefore, on behalf of all authors, the corresponding author states that there is no conflict of interest.

Acknowledgements

The Authors would like to acknowledge Dr. Iuri Boromei and Mr. Daniele Carosi of the Department of Industrial Engineering (DIN) at the University of Bologna (BO, Italy) for their invaluable contribution to the EBSD analysis (in the former case) and Hertzian contact stresses estimation in Scratch Test measurements (in the latter case); Ms. Anna Marzucco and Mr. Lorenzo Neri of The Great Romagna Hub Laboratory of Pievesestina in Cesena (FC, Italy) for their precious support to the antiviral evaluation of Cu-based materials. Special thanks also to Ms. Mariarosa Raimondo and Ms. Guia Guarini of the Institute of Science and Technology of Ceramic Materials (CNR-ISTEC, Faenza (RA)) for their necessary contribution to contact angle measurements and Ms. Giulia Maccaroni of the University of Bologna for her considerable efforts in the Cu-release quantification.

Pietro Galliani SpA funded Luca Lorenzetti's PhD grant within the Health & Technology PhD course of the University of Bologna, Italy.

References

[1] V. Govind, S. Bharadwaj, M.R. Sai Ganesh, J. Vishnu, K.V. Shankar, B. Shankar, R. Rajesh, Antiviral properties of copper and its alloys to inactivate covid-19 virus: a review, Biometals 34 (2021) 1217–1235, https://doi.org/10.1007/s10534-021-00339-4.

[2] S.L. Warnes, Z.R. Little, C.W. Keevil, Human coronavirus 229E remains infectious on common touch surface materials, mBio 6 (2015) 1–10, https://doi.org/10.1128/mBio.01697-15.

[3] S. Yezli, J.A. Otter, Minimum infective dose of the major human respiratory and enteric viruses transmitted through food and the environment, Food Environ. Virol. 3 (2011) 1–30, https://doi.org/10.1007/s12560-011-9056-7.

[4] C. Poggio, M. Colombo, C.R. Arciola, T. Greggi, A. Scribante, A. Dagna, Copper-alloy surfaces and cleaning regimens against the spread of SARS-CoV-2 in dentistry and orthopedics. From fomites to anti-infective nanocoatings, Materials 13 (2020) 1–12, https://doi.org/10.3390/ma13153244.

[5] K.A. Reynolds, P.I. Beamer, K.R. Plotkin, L.Y. Sifuentes, D.W. Koenig, C.P. Gerba, The healthy workplace project: reduced viral exposure in an office setting, Arch. Environ. Occup. Health 71 (2016) 157–162, https://doi.org/10.1080/19338244.2015.1058234.

[6] M. Nicas, D. Best, A study quantifying the hand-to-face contact rate and its potential application to predicting respiratory tract infection, J. Occup. Environ. Hyg. 5 (2008) 347–352, https://doi.org/10.1080/15459620802003896.

[7] V.C.C. Cheng, P.H. Chau, W.M. Lee, S.K.Y. Ho, D.W.Y. Lee, S.Y.C. So, S.C.Y. Wong, J.W.M. Tai, K.Y. Yuen, Hand-touch contact assessment of high-touch and mutual-touch surfaces among healthcare workers, patients, and visitors, J. Hosp. Infect. 90 (2015) 220–225, https://doi.org/10.1016/j.jhin.2014.12.024.

[8] N. van Doremalen, T. Bushmaker, D.H. Morris, M.G. Holbrook, A. Gamble, B.N. Williamson, A. Tamin, J.L. Harcourt, N.J. Thornburg, S.I. Gerber, J.O. Lloyd-Smith, E. de Wit, V.J. Munster, Aerosol and surface stability of SARS-CoV-2 as compared with SARS-CoV-1, N. Engl. J. Med. 382 (2020) 1564–1567, https://doi.org/10.1056/NEJMc2004973.

[9] C. Molteni, H.K. Abicht, M. Solioz, Killing of bacteria by copper surfaces involves dissolved copper, Appl. Environ. Microbiol. 76 (2010) 4099–4101, https://doi.org/10.1128/AEM.00424-10.

[10] S.J. Dancer, Importance of the environment in meticillin-resistant Staphylococcus aureus acquisition: the case for hospital cleaning, Lancet Infect. Dis. 8 (2008) 101–113, https://doi.org/10.1016/S1473-3099(07)70241-4.

[11] G. Grass, C. Rensing, M. Solioz, Metallic copper as an antimicrobial surface, Appl. Environ. Microbiol. 77 (2011) 1541–1547, https://doi.org/10.1128/AEM.02766-10.

[12] EPA Registers Copper Surfaces for Residual Use Against Coronavirus (2021). https://www.epa.gov/newsreleases/epa-registers-copper-surfaces-residual-use-against-coronavirus.

[13] S.L. Warnes, C.W. Keevil, Inactivation of norovirus on dry copper alloy surfaces, PLoS One 8 (2013), https://doi.org/10.1371/journal.pone.0075017.

[14] S.L. Warnes, S.M. Green, H.T. Michels, C.W. Keevil, Biocidal efficacy of copper alloys against pathogenic enterococci involves degradation of genomic and plasmid DNAs, Appl. Environ. Microbiol. 76 (2010) 5390–5401, https://doi.org/10.1128/AEM.03050-09.

[15] C.E. Santo, D. Quaranta, G. Grass, Antimicrobial metallic copper surfaces kill Staphylococcus haemolyticus via membrane damage, Microbiol. 1 (2012) 46–52, https://doi.org/10.1002/mbo3.2.

[16] D. Quaranta, T. Krans, C.E. Santo, C.G. Elowsky, D.W. Domaille, C.J. Chang, G. Grass, Mechanisms of contact-mediated killing of yeast cells on dry metallic copper surfaces, Appl. Environ. Microbiol. 77 (2011) 416–426, https://doi.org/10.1128/AEM.01704-10.

[17] C.E. Santo, E.W. Lam, C.G. Elowsky, D. Quaranta, D.W. Domaille, C.J. Chang, G. Grass, Bacterial killing by dry metallic copper surfaces, Appl. Environ. Microbiol. 77 (2011) 794–802, https://doi.org/10.1128/AEM.01599-10.

[18] J.L. Sagripanti, L.B. Routson, C.D. Lytle, Virus inactivation by copper or iron ions alone and in the presence of peroxide, Appl. Environ. Microbiol. 59 (1993) 4374–4376, https://doi.org/10.1128/aem.59.12.4374-4376.1993.

[19] M. Walkowicz, P. Osuch, B. Smyrak, T. Knych, E. Rudnik, Ł. Cieniek, A. Różańska, A. Chmielarczyk, D. Romaniszyn, M. Bulanda, Impact of oxidation of copper and its alloys in laboratory-simulated conditions on their antimicrobial efficiency, Corrosion Sci. 140 (2018) 321–332, https://doi.org/10.1016/j.corsci.2018.05.033.

[20] M. Hans, A. Erbe, S. Mathews, Y. Chen, M. Solioz, F. Mücklich, Role of copper oxides in contact killing of bacteria, Langmuir 29 (2013) 16160–16166, https://doi.org/10.1021/la404091z.

[21] Utilizing Antimicrobial Copper for Safer Communities, A Review of How Copper Can Reduce the Spread of Infection in Health and Pubblic Settings, Teck Resour. Ltd. KPMG, Antimicrob. Copp., 2021. https://www.teck.com/media/Copper.Health.White.Paper.Final.Teck.KPMG.pdf.

[22] T. Hallfeldt, W. Hotz, C. Leppin, S. Keller, H. Friebe, E.T. Till, R. Müller, M. Vučetić, H. Vegter, Sheet bulge testing, Compr. Mater. Process. 1 (2014) 85–93, https://doi.org/10.1016/B978-0-08-096532-1.00105-9.

[23] V.M. Villapún, S. Tardío, P. Cumpson, J.G. Burgess, L.G. Dover, S. González, Antimicrobial properties of Cu-based bulk metallic glass composites after surface modification, Surf. Coating. Technol. 372 (2019) 111–120, https://doi.org/10.1016/j.surfcoat.2019.05.041.

[24] T. Chang, M. Sepati, G. Herting, C. Leygraf, G.K. Rajarao, K. Butina, E. Blomberg, I.O. Wallinder, A novel methodology to study antimicrobial properties of high-touch surfaces used for indoor hygiene applications — a study on Cu metal, PLoS One 16 (2021) 1–25, https://doi.org/10.1371/journal.pone.0247081.

[25] V.M. Villapún, B. Qu, P.A. Lund, W. Wei, L.G. Dover, J.R. Thompson, J.O. Adesina, C. Hoerdemann, S. Cox, S. González, Optimizing the antimicrobial performance of metallic glass composites through surface texturing, Mater. Today Commun. 23 (2020) 101074, https://doi.org/10.1016/j.mtcomm.2020.101074.

[26] A.A. Cortes, J.M. Zuñiga, The use of copper to help prevent transmission of SARS-coronavirus and influenza viruses. A general review, Diagn. Microbiol. Infect. Dis. 98 (2020), https://doi.org/10.1016/j.diagmicrobio.2020.115176.

[27] C. Hewawaduge, A. Senevirathne, V. Jawalagatti, J.W. Kim, J.H. Lee, Copper-impregnated three-layer mask efficiently inactivates SARS-CoV2, Environ. Res. 196 (2021) 110947, https://doi.org/10.1016/j.envres.2021.110947.

[28] T. Chang, K. Butina, G. Herting, G.K. Rajarao, A. Richter-Dahlfors, E. Blomberg, I. Odnevall Wallinder, C. Leygraf, The interplay between atmospheric corrosion and antimicrobial efficiency of Cu and Cu5Zn5Al1Sn during simulated high-touch conditions, Corrosion Sci. 185 (2021) 109433, https://doi.org/10.1016/j.corsci.2021.109433.

[29] Asm International, J.R. Davi, in: Met Handb Desk (Ed.), Introduction and Overview of Copper and Copper Alloys, second ed., 2018, pp. 506–525, https://doi.org/10.31399/asm.hb.mhde2.a0003131.

[30] G. Simons, C. Weippert, J. Dual, J. Villain, Size effects in tensile testing of thin cold rolled and annealed Cu foils, Mater. Sci. Eng. 416 (2006) 290–299, https://doi.org/10.1016/j.msea.2005.10.060.

[31] T. Prasada Rao, M.C. Santhoshkumar, Highly oriented (1 0 0) ZnO thin films by spray pyrolysis, Appl. Surf. Sci. 255 (2009) 7212–7215, https://doi.org/10.1016/j.apsusc.2009.03.065.

[32] G.F. Vander Voort, Color metallography, in: Metallogr. Microstruct., ASM International, 2004, https://doi.org/10.31399/asm.hb.v09.a0003752.

[33] ASTM International, ASTM E2627–13 - Standard Practice for Determining Average Grain Size Using Electron Backscatter Diffraction (EBSD) in Fully Recrystallized Polycrystalline Materials, 2010, pp. 10–13, https://doi.org/10.1520/E2627-13R19.

[34] International Organization for Standardization, ISO 4288:1998 - Geometrical Product Specifications (GPS) - Surface Texture: Profile Method - Rules and Procedures for the Assessment of Surface Texture, 1998. https://bsol.bsigroup.com/.

[35] ASTM International, ASTM E92–17 - Standard Test Methods for Vickers Hardness and Knoop Hardness of Metallic Materials, 2017, pp. 1–27, https://doi.org/10.1520/E0092-17.

[36] International Organization for Standardization ISO, BS EN ISO 6507-1:2018 - Metallic Materials - Vickers Hardness Test, 2018. https://bsol.bsigroup.com/.

[37] International Organization for Standardization ISO, BS EN ISO 26424, Fine ceramics (advanced ceramics, advanced technical ceramics), Determination of the abrasion resistance of coatings by a micro-scale abrasion test (2016). https://bsol.bsigroup.com/.

[38] ASTM International, ASTM G171 - Standard Test Method for Scratch Hardness of Materials Using a Diamond Stylus, vols. 1–7, 2009, https://doi.org/10.1520/G0171-03R17.

[39] D.S. Asakawa, G.H. Crocker, A. Schmaltz, D.L. Jindrich, Fingertip forces and completion time for index finger and thumb touchscreen gestures, J. Electromyogr. Kinesiol. 34 (2017) 6–13, https://doi.org/10.1016/j.jelekin.2017.02.007.

[40] M. Ayyildiz, M. Scaraggi, O. Sirin, C. Basdogan, B.N.J. Persson, Contact mechanics between the human finger and a touchscreen under electroadhesion, Proc. Natl. Acad. Sci. U.S.A. 115 (2018) 12668–12673, https://doi.org/10.1073/pnas.1811750115.

[41] J.A. Williams, R.S. Dwyer-Joyce, Contact between solid surfaces, in: Mod. Tribol. Handb., CRC Press, 2001.

[42] N.C. Ammerman, M. Beier-Sexton, A.F. Azad, Growth and maintenance of Vero cell lines, Curr. Protoc. Microbiol. 11 (2008), https://doi.org/10.1002/9780471729259.mca04es11. A.4E.1–A.4E.7.
[43] C. Lei, J. Yang, J. Hu, X. Sun, On the calculation of TCID50 for quantitation of virus infectivity, Virol. Sin. 36 (2021) 141–144, https://doi.org/10.1007/s12250-020-00230-5.
[44] L.J. Reed, H. Muench, A simple method of estimating fifty per cent endpoints, Am. J. Epidemiol. 27 (1938) 493–497, https://doi.org/10.1093/oxfordjournals.aje.a118408.
[45] International Organization for Standardization ISO, BS EN 1811:2011+A1:2015 - Reference Test Method for Release of Nickel from All Post Assemblies Which Are Inserted into Pierced Parts of the Human Body and Articles Intended to Come into Direct and Prolonged Contact with the Skin, 2011. https://bsol.bsigroup.com/.
[46] S.L. Warnes, E.N. Summersgill, C.W. Keevil, Inactivation of murine norovirus on a range of copper alloy surfaces is accompanied by loss of capsid integrity, Appl. Environ. Microbiol. 81 (2015) 1085–1091, https://doi.org/10.1128/AEM.03280-14.
[47] R. Narayanasamy, R. Sowerby, Wrinkling of sheet metals when drawing through a conical die, J. Mater. Process. Technol. 41 (1994) 275–290, https://doi.org/10.1016/0924-0136(94)90166-X.
[48] S.L. Semiatin, Plastic deformation structures, ASM handbook, vol. 14A metalwork, Bulk Form 14 (2018) 539–551, https://doi.org/10.31399/asm.hb.v14a.a0004018.
[49] G.E. Totten, D.S. Mackenzie, Annealing and recrystallization of coppers, Heat Treat. Nonferrous Alloy. 4 (2018) 325–334, https://doi.org/10.31399/asm.hb.v04e.a0006278.
[50] F.J. Humphreys, M. Hatherly, Recrystallization and Related Annealing Phenomena, Pergamon, 2002, https://doi.org/10.1016/C2009-0-07986-0.
[51] K. Satoh, S. Sato, K. Yamanaka, S. Suzuki, A. Chiba, K. Wagatsuma, Line-profile analysis combined with texture analysis for characterizing dislocation distribution in texture components of cold-rolled copper sheets, High Temp. Mater. Process. 35 (2016) 705–713, https://doi.org/10.1515/htmp-2015-0039.
[52] G. Benchabane, Z. Boumerzoug, I. Thibon, T. Gloriant, Recrystallization of pure copper investigated by calorimetry and microhardness, Mater. Char. 59 (2008) 1425–1428, https://doi.org/10.1016/j.matchar.2008.01.002.
[53] M. Liu, Microscratch of copper by a Rockwell C diamond indenter under a constant load, Nanotechnol. Precis. Eng. 4 (2021), https://doi.org/10.1063/10.0005065.
[54] K.J. Vannoy, J.E. Dick, Oxidation of cysteine by electrogenerated hexacyanoferrate(III) in microliter droplets, Langmuir 38 (2022) 11892–11898, https://doi.org/10.1021/acs.langmuir.2c01385.
[55] S.D. Walji, M.R. Bruder, M.G. Aucoin, Virus matrix interference on assessment of virucidal activity of high-touch surfaces designed to prevent hospital-acquired infections, Antimicrob. Resist. Infect. Control 10 (2021) 1–12, https://doi.org/10.1186/s13756-021-01001-x.
[56] N. Fredj, J.S. Kolar, D.M. Prichard, T.D. Burleigh, Study of relative color stability and corrosion resistance of commercial copper alloys exposed to hand contact and synthetic hand sweat, Corrosion Sci. 76 (2013) 415–423, https://doi.org/10.1016/j.corsci.2013.07.015.
[57] S. Colin, E. Beche, R. Berjoan, H. Jolibois, A. Chambaudet, An XPS and AES study of the free corrosion of Cu-, Ni- and Zn-based alloys in synthetic sweat, Corrosion Sci. 41 (1999) 1051–1065, https://doi.org/10.1016/S0010-938X(98)00141-3.
[58] I. Salah, I.P. Parkin, E. Allan, Copper as an antimicrobial agent: recent advances, RSC Adv. 11 (2021) 18179–18186, https://doi.org/10.1039/d1ra02149d.
[59] N. Gugala, J.A. Lemire, R.J. Turner, The efficacy of different anti-microbial metals at preventing the formation of, and eradicating bacterial biofilms of pathogenic indicator strains, J. Antibiot. (Tokyo) 70 (2017) 775–780, https://doi.org/10.1038/ja.2017.10.
[60] A.F. Murray, D. Bryan, D.A. Garfinkel, C.S. Jorgensen, N. Tang, W. Liyanage, E.A. Lass, Y. Yang, P.D. Rack, T.G. Denes, D.A. Gilbert, Antimicrobial properties of a multi-component alloy, Sci. Rep. 12 (2022) 1–14, https://doi.org/10.1038/s41598-022-25122-4.
[61] D. Wojcieszak, D. Kaczmarek, A. Antosiak, M. Mazur, Z. Rybak, A. Rusak, M. Osekowska, A. Poniedzialek, A. Gamian, B. Szponar, Influence of Cu-Ti thin film surface properties on antimicrobial activity and viability of living cells, Mater. Sci. Eng. C 56 (2015) 48–56, https://doi.org/10.1016/j.msec.2015.06.013.
[62] V.M. Villapún, L.G. Dover, A. Cross, S. González, Antibacterial metallic touch surfaces, Materials 9 (2016) 1–23, https://doi.org/10.3390/ma9090736.
[63] C. Li, J. Zhang, J. Han, B. Yao, A numerical solution to the effects of surface roughness on water–coal contact angle, Sci. Rep. 11 (2021) 1–12, https://doi.org/10.1038/s41598-020-80729-9.